Macromolecules
ARTICLE

Macromolecules **2009**, *42*, 8933–8942 **8933**
DOI: 10.1021/ma901671v

ZnO Nanorod−Thermoplastic Polyurethane Nanocomposites: Morphology and Shape Memory Performance

Hilmar Koerner,[†,§] John Kelley,[†] Justin George,[†] Lawrence Drummy,[†] Peter Mirau,[†] Nelson S. Bell,[‡] Julia W. P. Hsu,[‡] and Richard A. Vaia*[,†]

[†]*Materials and Manufacturing Directorate, Air Force Research Laboratory, AFRL/RXBN, 2941 Hobson Way, Wright-Patterson AFB, Ohio 45433,* [‡]*Center for Integrated Nanotechnologies, Sandia National Laboratories, Albuquerque, New Mexico, 87185, and* [§]*Universal Technology Corporation, Dayton, Ohio, 45432*

Received July 28, 2009; Revised Manuscript Received September 25, 2009

ABSTRACT: The impact of dispersed alkylthiol-modified ZnO nanorods, as a function of rod aspect ratio and concentration, on the shape memory character of a thermoplastic polyurethane with low hard-segment density (LHS-TPU) is examined relative to the enhanced performance occurring for carbon nanofiber (CNF) dispersion. Solution blending resulted in uniform dispersion within the LHS-TPU of the ZnO nanorods at low volume (weight) fractions ($<2.9\%$ v/v (17.75% w/w)). Tensile modulus enhancements were modest though, comparable to values observed for spherical nanofillers. Shape memory characteristics, which in this LHS-TPU result when strain-induced crystallites retard the entropic recovery of the deformed chains, were unchanged for these low volume fraction ZnO nanocomposites. Higher ZnO loadings (12% v/v (50% w/w)) exhibited clustering of ZnO nanorods into a mesh-like structure. Here, tensile modulus and shape recovery characteristics were improved, although not as great as seen for comparable CNF addition. Wide angle X-ray diffraction and NMR revealed that the addition of ZnO nanorods did not impact the inherent strain induced crystallization of the LHS-TPU, which is in contrast to the impact of CNFs and emphasizes the impact of interactions at the polymer−nanoparticle interface. Overall, these findings reinforce the hypothesis that the shape memory properties of polymer nanocomposites are governed by the extent to which nanoparticle addition, via nanoparticle aspect ratio, hierarchical morphology, and interfacial interactions, impacts the molecular mechanism responsible for trapping elastic strain.

Introduction

Shape memory polymers (SMPs) are being increasingly examined for technologies ranging from biomedical implants to morphing structures due to their ability to recover deformations $>500\%$ or exert recovery stresses of up to 5 MPa[1,2] A SMP's permanent shape is initially established by either chemically or physically cross-linking. In the latter case, the transition temperature associated with the physical cross-link is much greater than the maximum operating temperature of the SMP. The temporary shape is trapped by a mechanism that inhibits relaxation of the polymer chains after initial deformation. Two general classes of SMPs can be identified based on the molecular mechanism that acts to retard the recovery of this elastic strain energy.[3,4] This "locking in" can occur either via a thermal quench or the further in situ creation of reversible physical cross-links, such as crystallites or a microphase transition. For the former SMP class, exemplified by cross-linked polynorbornene and epoxy resins, the temporary shape is created by deforming the permanent shape slightly above the glass transition temperature (T_g), followed by a temperature decrease to below T_g. Shape recovery occurs upon reheating above the T_g; thereby allowing relaxation of the deformed chains. In contrast, the latter class of SMPs, such as cross-linked polyethylene and microphase separated thermoplastic polyurethanes, can be "cold-drawn"[5] to set a temporary shape.[6] These materials undergo crystallization upon deformation at temperatures between T_g and the melting point of the crystalline phase (T_m). These newly formed crystallites immobilize polymer chains and aid in "locking in" the temporary shape. Heating above T_m releases these constraints, allowing entropic recovery of the chains, and return of the system to its original shape.[6] In general, these two mechanisms can be combined to provide a rich array of possible shape programming-recovery methodologies.

Substantial research, ranging from the modification of the chemical structure of the polymer chain[7] to copolymerization, blending and altering cross-link density,[2] has been conducted to enhance various facets of the shape memory character of these two general classes.[4,8,9] Today, a large family of polymers is available; however creep, restricted operating temperatures, insufficient precision in setting the temporary shape, low thermal conductivity, and minimal stress generation challenge implementation of shape memory polymers into systems requiring substantial robustness, such as morphing or deployable structures.

A potential approach to address these limitations and create stronger, tougher materials is through the addition of inorganic particles, ranging from micro-[10] to nanoscale.[11,12,6] Gall and coworkers were one of the first to report the use of nanoparticles to modify shape memory polymers.[13] Increase of the constrained bending recovery by 50% however required substantial addition of SiC (>20 wt %) to the shape memory epoxy. Other efforts examining T_g-based SMPs have supported these observations.[14] Such high loadings unfortunately lead to reduced elongation and toughness.[15] This impact on shape memory behavior can normally be attributed to the relatively minor impact of nanofillers on the chain dynamics associated with the glass transition temperature, T_g. Shifts of T_g of 5−10 °C are compensated by

*Corresponding author. E-mail: richard.vaia@wpafb.af.mil.

Published on Web 10/07/2009

minor changes in the temperature program of the setting protocol. In contrast, nanocomposites incorporating anisotropic nanoparticles (e.g., carbon nanotubes) within a strain-induced crystallizable SMP matrix have shown promising improvements of fixity and stress recovery.[6,16] In this instance, the carbon nanotubes substantially altered the molecular mechanism underlying shape retention, that is strain-induced crystallization, as well as increasing the modulus of the polymer throughout the shape-setting and recovery processes. Comparable improvements were not observed for spherical fillers, such as carbon black, even at high loadings. This implied that aspect ratio of the filler was the key parameter in this class of nanocomposite SMPs. Irrespective of the impact on shape memory character, the addition of nanoparticles has provided novel routes for heating the SMP (Joule heating,[6] IR light,[6,17] RF[18] or magnetic fields[19]). These alternatives to traditional radiative or contact heating to trigger shape recovery are currently driving commercial development of nanocomposites SMPs.[20,21]

In order to further the understanding of how nanoparticle shape and dispersion impacts the mechanical aspects of SMPs, we have investigated the morphology and shape memory response of a low hard-segment thermoplastic polyurethane filled with ZnO nanorods of different aspect ratio. ZnO nanoparticles are readily synthesized into a variety of shapes, including spheres, ribbons, wires or rods.[22] Previous work on polymers containing dispersed ZnO nanospheres have examined their impact on mechanical and optical properties, as well as their effect on polymer crystallization.[23−26] The thermal[27] and optical properties[28] of nanocomposites prepared with ZnO nanorods have also been reported. Building on our previous investigation of carbon nanofibers (CNF) addition to thermoplastic polyurethane, ZnO nanorods with different aspect ratios expand the understanding of how concentration, particle shape, surface chemistry, and distribution of nanofiller impacts the critical properties (modulus, stiffness, and crystallization) that determine the shape memory response for strain-induced crystallizable SMPs.

Experimental Section

ZnO Nanorod Synthesis. ZnO nanorod synthesis followed published procedures.[29,30] In brief, 8.7807 g of zinc acetate dehydrate (Aldrich, 98%) was refluxed under flowing nitrogen in 200 mL anhydrous ethanol (Aldrich) for 3 h, forming a transparent solution. The solution was allowed to cool to approximately 40 °C, and added to a Teflon liner for a Parr instruments hydrothermal vessel (600 mL, Model 4560 mini Bench Top Reactor, Parr Instruments, Moline, IL 61265). A second solution was made using 2.256 g KOH (Aldrich, ACS grade) in 100 mL of anhydrous ethanol and dissolved using an ultrasonic bath. To this solution, 3 mL of ethylenediamine was added. The second solution was added to the zinc acetate solution in the pressure vessel, forming a white precipitate immediately. The chamber was sealed, and nitrogen was bubbled through the reaction chamber for 5 min to remove air. The stirring motor for the vessel was set to 100 rpm during the thermal reaction program. The thermocontroller for the pressure vessel performed a heating profile of a 60 min ramp from room temperature to 120 °C, followed by a hold at 120 °C for 960 min, and ending with power shutoff and uncontrolled cool down to ambient temperature. The resulting ZnO nanorod precipitate was recovered using four cycles of centrifugation and redispersion in ethanol. Residual water content and kinetic factors in the dissolution and growth of the ripening nuclei determine the aspect ratio, α. SEM of precipitated samples with short (ZnO-S, 11 × 54 nm, $\alpha \sim 5$) and long (ZnO-L, 13 × 143 nm, $\alpha \sim 10$) ZnO rods are shown in Figure 1, parts a and b. A high resolution TEM of a single ZnO rod revealed the internal crystal structure (002 lattice planes) confirming its single crystal nature (Figure 1c). Note that ZnO size is approximate. Both TEM and SEM analysis indicate a very broad size distribution both in thickness and length (±40%).

To prevent aggregation and improve dispersion in the polymer matrix, zinc oxide nanorods were surface functionalized with 1-dodecanethiol (Aldrich). Thiol surface functionalization of ZnO nanoparticles is well established in the growth process of ZnO nanoparticles in which thiols act as capping agents.[31] The ethanol solutions from ZnO nanorods synthesis were determined to be 5.5 wt % ZnO nanorods by solvent evaporation method. To 10 mL of the ZnO-ethanol solutions, 222 μL of dodecanethiol were added. The suspensions were agitated using an ultrasonic bath, and allowed to react at room temperature overnight. The solutions were tested for stability by adding 1 mL of toluene to each sample, and aggregation was not observed in either sample. Note that pristine ZnO nanorods precipitate from THF solutions, and when combined with LHS-TPU, resulted in large (>1 μm) agglomerates.

Nanocomposite Fabrication. The neat thermoplastic polyurethane was supplied by Huntsman Polyurethanes (Irogran PS455−203, in the following referred to as LHS-TPU). The LHS-TPU contains 9.9% 4−4′-methylenediphenylene isocyanate (MDI), 58.2% butyl−diol, and 31.8% adipate segments[16] (Figure 1d). Previous proton NMR resolved the alkyl chain length and distribution of lengths of the diacid and diol segments, and the relative fraction of distinct protons indicates that the LHS-TPU contains ~90% diol/diacid soft segments. Detailed summary of the physical characteristics of LHS-TPU can be found elsewhere.[32] Heat treated CNF (PRT-HT-19) were obtained from Applied Science Inc. and exhibit a diameter between 60 and 100 nm and a length up to 10 μm, resulting in $\alpha \sim 100$. In addition to a substantially higher α, the CNF surface contains carbonyl and phenolic groups which are more amenable to hydrogen bonding with urethane linkages than the alkylated ZnO surface.

Samples were prepared to match concentrations based on already available data from carbon nanofiber - LHS-TPU nanocomposites: 1 (0.5), 5 (2.9), and 17.8 (11) % w/w (% v/v).[16] Weighed quantities of these dispersions provided the necessary amount of ZnO to afford 2.5 (0.35), 17.75 (2.9) and 50 (12) % w/w (% v/v) dispersions in the LHS-TPU. The mixture was diluted in 5 mL of THF, stirred, and agitated via ultrasonication. Films of the dispersions were cast into Teflon molds (100 mm x 25 mm x 20 mm) and allowed to slowly evaporate. The evaporated films were dried in vacuum (4 mbar) at 75 °C. Film thicknesses ranged from 0.15 to 0.25 mm. Nanocomposites will be referred to as follows: NP#, where NP corresponds to the nanoparticle (ZnO-S ($\alpha = 5$), ZnO-L ($\alpha = 10$), CNF) and # corresponds to the volume percentage (% v/v).

Note that previous reports have indicated that modifiers such as alkyl thiols at elevated concentration (>4%) may act as a plasticizer and/or crystallite inhibitor; thus reducing stiffness and imparting enhanced strain-to-break.[33,34] For the ZnO nanocomposites discussed here, however, the addition of the dodecanethiol surfactant directly to neat LHS-TPU of a concentration in excess of that contained in the ZnO nanocomposites (<2%) did not alter the mechanical properties, nor crystallite content and morphology.

Transmission Electron Microscopy and X-ray Diffraction. Films were embedded in a two-part epoxy and trimmed for cross-sectioning. For longitudinal (in-plane) film sectioning, films were mounted on the surface of an epoxy block using superglue and trimmed for microtomy. Ultrathin sections for TEM were cut using a RMC PowerTome XL cryo-ultramicrotome equipped with a Diatome diamond knife. Samples were cooled below the glass transition of the polymer during cutting (−130 °C), and a speed of 1 mm/sec was used to cut 50 −100 nm thick sections. Sections were then collected on 400 mesh copper grids. TEM was performed on a Philips CM 200 operating at 200 kV and images were recorded using a CCD camera.

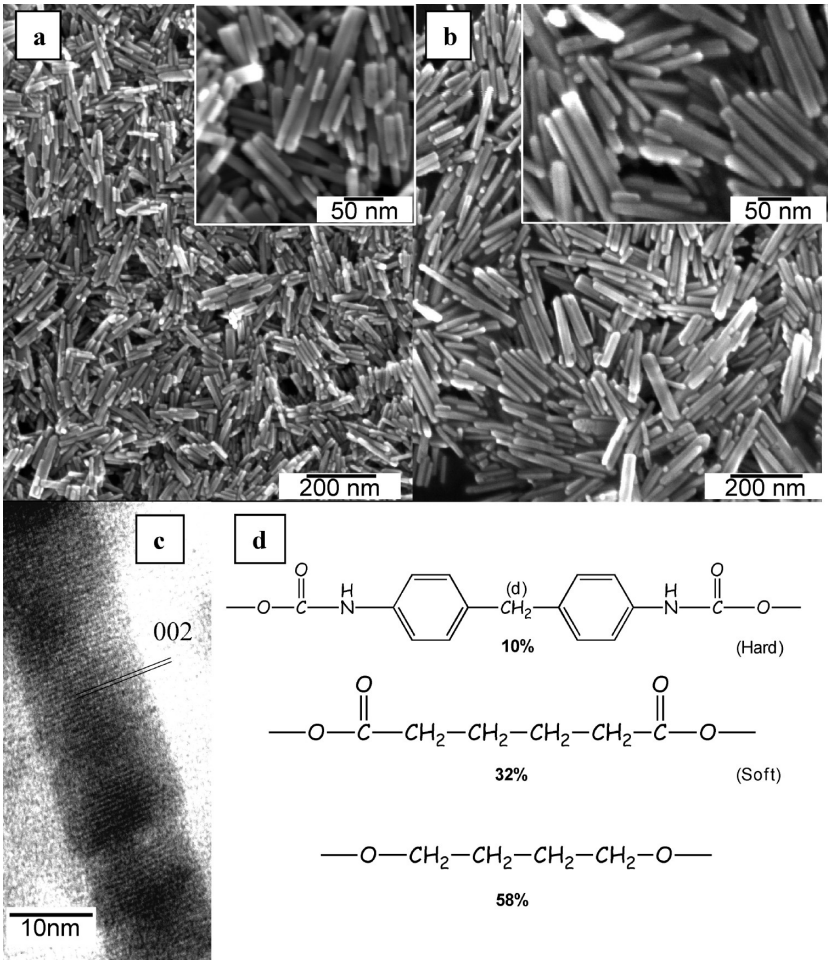

Figure 1. Scanning electron micrograph of (a) ZnO-S (11 × 54 nm) nanorods and (b) ZnO-L (13 × 143 nm) nanorods. (c) High resolution transmission electron micrograph of internal crystal lattice (002) of a ZnO nanorod. (d) Chemical structure of the segments of LHS-TPU (Irogran PS455−203; hard segment = 10% isocyanate; soft segments = 32% adipate and 58% butyl diol).

X-ray diffraction was conducted on a Bruker AXS D8 Discover and Statton box camera in transmission mode. Hermans orientation parameters were calculated according to standard procedures[35] from azimuthal integration of diffraction peaks. Deformation-morphology correlations were determined using synchrotron X-ray experiments, conducted at X27C, National Synchrotron Light Source at Brookhaven National Laboratory. Sample to detector distance was 164 mm (WAX), 1800 mm (SAX) at a wavelength of 0.1371 nm, defined by a double multilayer monochromator. The synchrotron X-rays were collimated to a 600 μm beam size using a three-pinhole collimator. WAX and SAX images were obtained using a Mar CCD detector. 40 × 4x0.5 mm samples were mounted in a modified Instron that allows uniaxial, symmetrical extension to expose the gauge section of the sample to the X-ray beam.

Solid State Proton NMR. Solid-state carbon NMR spectra were acquired at 125 MHz using a Tecmag Apollo 500 NMR spectrometer. The polymer and ZnO/polymer films were packed into 5 mm rotors for signal acquisition with magic-angle sample spinning and high power decoupling using a Doty XC5 probe. The carbon spin−lattice (T_1) relaxation times were measured using the inversion recovery pulse sequence,[36] and the chemical shifts were referenced to an external sample of hexamethylbenzene at 17.35 ppm. The carbon and proton fields were set to 50 kHz and the spectra were acquired with two-pulse phase-modulated decoupling.[37]

Mechanical and Shape Memory Characterization. Tensile tests and constrained stress recovery experiments were conducted on a Tinius Olson H10KS benchtop tensile tester on a nominal sample size of 25.4 × 4 × 0.4 mm average. A stretching force was applied to one pneumatic clamp. Clamp displacement was used to determine elongation ratio and engineering strain. Engineering stress was calculated from the initial cross-sectional area of the sample. A limitation of engineering strain typically occurs when polymers exhibit necking. We did not observe necking of the samples at any strain within this work. Samples were deformed (rates: 20 mm/min) to the initial setting strain and held at constraint strain for 1 min, during which the initial stress relaxed. Samples were further relaxed (rate: 30 mm/min) to zero force. The amount of strain relaxation to an equilibrated deformation before determination of stress recovery is reported as constrained fixity f_{SM}, which is the ratio of initial strain set to the strain that can be retained by the system after removal of stress without heating. Thermal actuation at constant strain was conducted using controlled convective heating with a thermocouple at the sample surface. Temperature and heating rates were kept constant (10 °C /min, final 65 °C for 1 min, subsequent cooling after recovery for 2 min.). Note that constrained fixity as determined in the constrained stress recovery experiment is distinct from shape memory fixity (the amount of initial deformation that is recoverable), which reflects the free strain behavior of the material.[38] Shape memory recovery stress, s_{SM}, is the amount of stress on the tensile load cell that the sample exerts when recovery is triggered at a fixed strain. The recorded stress reaches a peak and then decays into a constant plateau value within 1 min, which is the value reported as s_{SM}. Here, this fixed strain is that of the temporary shape resulting from the tensile deformation of the permanent shape. Shape memory recovery

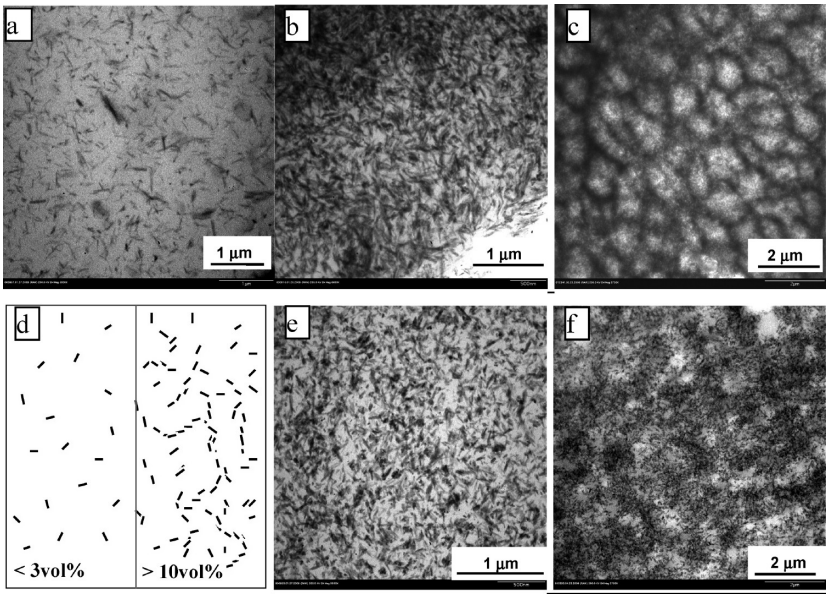

Figure 2. Transmission electron microscopy of ZnO/LHS-TPU nanocomposite series: (a) ZnO-L0.35; (b) ZnO-L2.9; (c) ZnO-L12; (e) ZnO-S2.9; (f) ZnO-S12. (d) Schematic of low and high loading ZnO nanocomposite morphology.

stress reflects the maximum force output available from the material based on the original cross-sectional area. Constrained shape memory fixity and stress recovery data were obtained on multiple (8) specimens for each sample. Standard deviations between samples were ~10%. The reported shape memory parameters reflect the average of 10 set-recover cycles beginning at the third cycle. The initial cycles for both filled and unfilled decay substantially and depend on prior sample history.[6] Constrained fixity and stress recovery data is constant in subsequent cycles.

Results and Discussion

The mechanical characteristics of nanocomposites based on semicrystalline and microphase-separated polymers are known to be sensitive to both the distribution of the nanoparticles as well as the impact of particle dispersion on the morphology of the polymer matrix.[39]

Nanocomposite Morphology. Excellent dispersion of the ZnO nanorods was achieved via the simple solution mixing of nanorod dispersions with LHS-TPU in THF. Optical microscopy of the dried films show uniform textures, with lower concentrations appearing semitransparent and higher concentrations white. Figure 2 summarizes representative transmission electron micrographs of the nanocomposites with varying ZnO concentrations. At the lower concentrations (<2.9 vol %), individual and small clusters (2−4) of ZnO nanorods are dispersed uniformly throughout the LHS-TPU. At the highest concentration (12 vol %), microphase separation of the nanorods occurs, resulting in a three-dimensional mesh structure of ZnO-rich regions (~100−200 nm) surrounding pockets (~0.5−1 μm) of well dispersed nanorods and small clusters. The hierarchical structure is more developed for the longer nanorods (ZnO-L) than the shorter nanorods (ZnO-S). This morphology is suspected to arise from attractive interactions between closely packed nanorods[40] and is qualitatively similar to recent reports of sheet and rod-like agglomerates of nanosilica in polystyrene.[41] At higher loadings, the effectively reduced mean particle−particle distance increases the probability of cluster formation prior to solvent induced gelation, potentially leading to the extended structures. These ZnO structures are most-likely kinetically trapped due to the large thermal energy necessary for Brownian motion of these particles in a matrix of such high viscosity, the physically cross-linked polymer network arising from segregation of the LHS-TPU hard-segments, and the absence of prolonged elevated temperature anneals in the processing protocol.

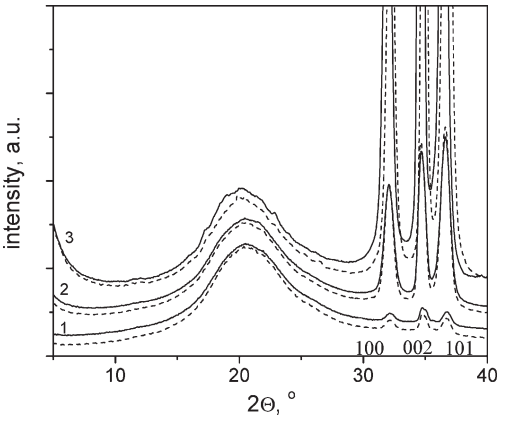

Figure 3. Wide angle X-ray diffraction of unstretched (λ = 1) ZnO - LHS-TPU nanocomposites: (1) ZnO-L0.35 and ZnO-S0.35; (2) ZnO-L2.9 and ZnO-S2.9; (3) ZnO-L12 and ZnO-S12 where the dashed curves are ZnO-L and the solid curves are ZnO-S.

In many instances, the concentration, structure and morphology of the crystal phase of semicrystalline polymers are impacted by the presence of nanofillers.[42] For example, dispersion of organically modified layered silicate (nanoclay) is known to alter the crystal content and habit of nylon-6[43] and PVDF.[44,45] Figure 3 shows the wide-angle X-ray scattering of the LHS-TPU nanocomposites. The sharp reflections between 2θ = 30° and 40° arise from the crystal lattice of the ZnO nanorods and the intensity of these reflections is directly proportional to the concentration of ZnO nanorods. The broad peak at approximately 2θ = 20° arises from the amorphous regions of the polymer. Deconvolution of this broad reflection reveals a small feature at 2θ = 22° which from previous studies is assigned to the crystalline phase of the soft-segments of the LHS-TPU.[32] Using these reflections, the crystallinity index (X) of unfilled

LHS-TPU is < 2% and in agreement with previous DSC and X-ray data of solution cast LHS-TPU films.[32] The crystallinity index of LHS-TPU in all ZnO nanocomposites reported here is similar to the unfilled LHS-TPU, irrespective of nanorod concentration or size. This indicates that the dodecanethiol functionalized nanorods do not impact the soft-segment crystallite formation during solvent removal or cooling through the soft segment melting point (T_{ms} = 48 °C). This is in contrast to previous reports for carbon nanotube LHS-TPU nanocomposites.[6,17,18] In one example upon solvent removal from the 2.9 vol % CNF nanocomposite, crystallinity was increased over 7-fold (X ~15.2%). Note that the amount of soft-segment crystallinity can be controlled by thermal cycling as-cast samples above T_{ms}, followed by controlled cooling to ambient as done for samples discussed herein.

High-resolution solid-state NMR and carbon spin−lattice relaxation studies further confirm that the ZnO nanorods have at most a minor impact on the structure and local segmental relaxation dynamics of the LHS-TPU matrix. The similarity between the chemical shifts and line widths of the carbon spectrum (Figure 4) from neat LHS-TPU and ZnO-L2.9 nanocomposite indicates the local environment of the rigid (glassy) phases are unchanged by addition of ZnO.[36] The peaks at 173, 64, 34, and 26 ppm are assigned to carbonyl carbons, methylene carbons near oxygen and methylene carbons in the soft segments, respectively.[16] Note that the methylene carbons associated with the dodecanethiol surface functionalization on the ZnO are of insufficient quantity to be observed. Carbon spin−lattice relaxation times, which are sensitive to molecular motions near the inverse of the carbon frequency (125 MHz), were also similar for neat LHS-TPU and ZnO nanocomposite (Table 1).[36] Long T_1's are observed for very fast or very slow molecular motion, while a minimum in the T_1 is observed for large amplitude motion near the carbon frequency. The longest T_1's (2.0−3.0 s) are observed for the carbonyl carbons which do not have directly attached protons, where as the minimum T_1's (0.20−0.35 s) are observed for the methylene carbons. Overall, the NMR indicates that the polymer chain is very mobile at room temperature, and that the average mobility is not impacted by the presence of 12 vol % of the ZnO nanoparticles, corroborating the X-ray scattering observations.

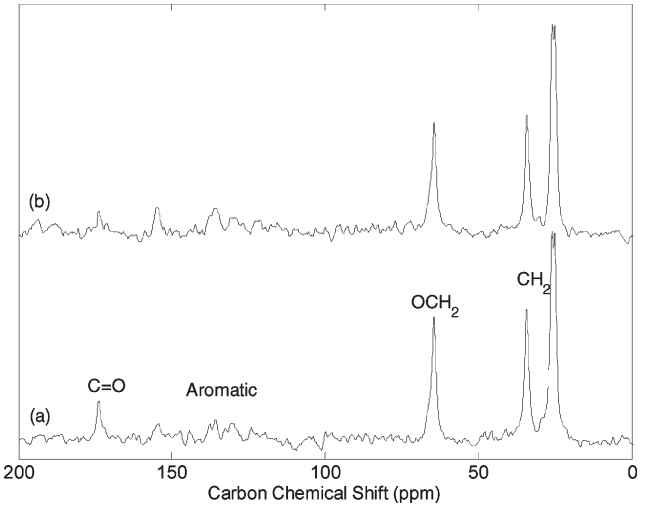

Figure 4. The 125 MHz solid-state carbon NMR spectra of (a) the LHS-TPU and (b) ZnO-L2.9 nanocomposite obtained with cross-polarization and magic-angle sample spinning.

Overall, the NMR studies, as with the XRD, are in contrast to prior studies on CNF LHS-TPUs.[46] CNF addition lead to changes in both the chemical shifts and line widths of the mobile phase, supporting a model in which nucleation of a crystalline phase is promoted at the surface of the CNFs. The tendency for the CNFs to promote crystallization relative to the ZnO is believed to reflect the different surface chemistries. The CNF surface, which contains carbonyl and phenolic groups, is more favorable to hydrogen bonding than that of the alkylated ZnO nanorods, thus more likely to promote heterogeneous nucleation.

In summary, TEM, XRD, and NMR indicate that the presence of small to intermediate amounts of ZnO nanorods does not alter the morphology and local molecular relaxation behavior of the LHS-TPU. At high nanofiller loadings TEM indicates ZnO nanorods cluster into a hierarchical mesh-like morphology, rather than the uniform dispersion observed at lower loadings.

Deformation Characteristics. Figure 5 and Table 2 summarize the stress response due to uniaxial extension, as well as tensile modulus, stress-at-break and strain-at-break for the ZnO nanocomposites. For comparison, the mechanical

Table 1. Carbon Spin−Lattice Relaxation Times (s) for the Polymer and the 2.9 vol % ZnO-L LHS-TPU Nanocomposite

sample	δ_C = 173 ppm	δ_C = 64 ppm	δ_C = 34 ppm	δ_C = 26 ppm
LHS-TPU	2.0	0.26	0.26	0.22
ZnO-L2.9	2.2	0.24	0.23	0.20
ZnO-L12	3.0	0.27	0.35	0.25
ZnO-S12	2.4	0.29	0.32	0.26

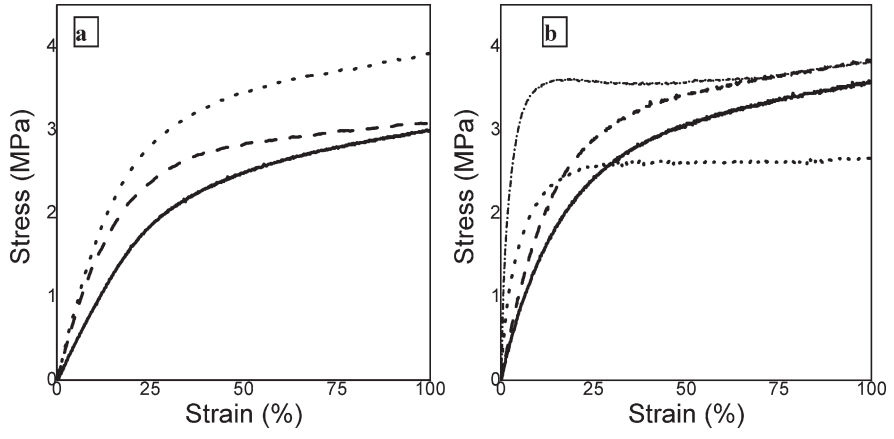

Figure 5. Stress strain plots for ZnO nanocomposites. Key: (a) (—) neat LHS-TPU; (− −) ZnO-L0.35; (· · ·) ZnO-S0.35; (b) (− −) ZnO-L2.9; (—) ZnO-S2.9; (− · −) ZnO-L12; (· · ·) ZnO-S12.

Table 2. Tensile Modulus, Engineering Stress at Failure, and Engineering Strain at Failure

	tensile modulus, E (MPa)	stress at failure, σ_F (MPa)	strain at failure, ε_F (%)
LHS-TPU	13 ± 2	26.2 ± 5	1352 ± 110
ZnO-S0.35	18.1 ± 5	28.0 ± 4	1356 ± 190
ZnO-L0.35	16.2 ± 3	21.9 ± 4	1199 ± 100
ZnO-S2.9	16.8 ± 5	21.3 ± 4	1368 ± 150
ZnO-L2.9	18.1 ± 6	26.7 ± 7	1535 ± 210
ZnO-S12	79.2 ± 8	12.0 ± 4	1059 ± 220
ZnO-L12	162.9 ± 35	8.7 ± 1	669 ± 200
CNF-2.9	55 ± 5	22 ± 2	1050 ± 100
CNF-11	130 ± 10	27 ± 3	1200 ± 120

characteristics of CNF nanocomposites are included, in which the solvent-cast soft-segment crystallites were thermally erased. At concentrations less than 2.9 vol %, the tensile modulus, E, of ZnO nanocomposites only increased from 13 to 17 MPa, where as the strain softening behavior and failure characteristics were qualitatively unchanged. Both long and short ZnO nanorods had similar impact at these loadings. Only at the highest loadings (12 vol %) was the modulus enhancement appreciable. Additionally, a distinct yield event and associated yield stress, σ_y, develops around 17−20% strain followed by an approximately strain-independent flow stress not observed in either the neat matrix or the lower loaded ZnO nanocomposites. In conjunction with this change in deformation character, the average strain, ε_F, and stress, σ_F, at failure for these nanocomposites decreased relative to unfilled LHS-TPU. Furthermore, at these loadings the impact of ZnO nanorod size, or more likely the resultant hierarchical morphology, is pronounced. The greater yield stress of ZnO-L12 is accompanied by lower extensibility (ε_F) and a lower stress at failure σ_F relative to ZnO-S12. This inverse relationship between strength and toughness at high inorganic filler concentration is consistent with numerous prior nanocomposite reports, where the cohesive failure of the highly stressed matrix regions between filler particles can result in reduced strain at break.[47]

A key contribution to the reinforcement below the percolation limit of soft elastomeric materials, such as LHS-TPU, at strains of 10−30% is "hydrodynamic"[48] or "strain"[49] amplification, in which the polymer chains surrounding a rigid inclusion experience a local microscopic strain that is in excess of the macroscopic external strain. Concentration and aspect ratio of an anisotropic filler particle are the most important contributors to determining the extent of reinforcement under these loading conditions. The impact of fillers as diverse as carbon black[50] to carbon nanofibers and layered silicates[51] can be semiquantitatively described by relationships proposed by Guth,[48] Gold,[52] and Boyce and co-workers[53] and is typically expressed as the ratio of moduli between composite (E) and the matrix (E_m). The ZnO-LHS-TPU nanocomposites at lower loadings (ϕ < 2.9 vol %) show enhancements ($E/E_m|_{\text{ZnO-LHS-TPU, }\phi=0.03} \sim 1.3$) anticipated for rods with aspect ratios α, between 5 and 10 ($E/E_m|_{\alpha=10,\ \phi=0.03} \sim 1.3$, as estimated from the Guth model). At these loadings, the enhancements are only marginally improved to that observed for spherical fillers ($E/E_m|_{\text{sphere, }\phi=0.03} \sim 1.1$). In comparison, enhancements for CNF nanocomposites at these loadings were found to be much larger ($E/E_m|_{\text{CNF-LHS-TPU, }\phi=0.03} \sim 4$). At the highest loadings though, the enhancement for ZnO-L addition ($E/E_m|_{\text{ZnO-LHS-TPU, }\phi=0.12} \sim 12$) is greater than anticipated for $\alpha \sim 10$ ($E/E_m|_{\alpha=10,\ \phi=0.12} \sim 4.1$, as estimated from the Guth model) and similar to carbon nanofibers ($E/E_m|_{\text{CNF-LHS-TPU, }\phi=0.11} \sim 10$). Although not as great of an enhancement, the ZnO-S addition of 12 vol % is also greater than anticipated.

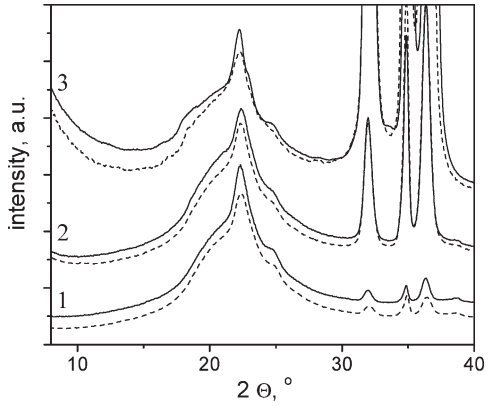

Figure 6. Wide angle X-ray diffraction of stretched (λ = 3.5) ZnO-LHS-TPU nanocomposites. Key: (1) ZnO-L0.35 (X = 16.7%) and ZnO-S0.35 (X = 14.3%); (2) ZnO-L2.9 (X = 14.9%) and ZnO-S2.9 (X = 15.0%); (3) ZnO-L12 (X = 16.0%) and ZnO-S12 (X = 15.1%) where the dashed curves are ZnO-L and the solid curves are ZnO-S. X represents the relative crystallinity determined from the patterns. For reference at λ = 3.5, X = 15% for LHS-TPU and X = 25% for CNF-2.9.

The origin of the modulus behavior likely arises from the morphology differences (Figure 2d) between low and high ZnO content, since the addition of ZnO nanorods does not alter the inherent crystallite content of the polymer matrix. At the lowest loadings, the ZnO nanorods are approximately isolated and not arranged into extended structures, which is consistent with the assumption of isolated rigid units for the hydrodynamic concepts underlying the aforementioned models. In contrast, the higher loading nanocomposites exhibit a percolative network morphology, which is not consistent with this assumption. Furthermore, the framework morphology in ZnO-L nanocomposites is more developed than in the ZnO-S nanocomposites, consistent with greater low strain reinforcement. As discussed in prior work[54] and reduced to practice in lightweight, honeycomb core composites,[55] a three-dimensional network of rigid members or clustered rigid particles that span the sample can efficiently increase composite rigidity at a lower volume loading than anticipated for uniformly dispersed units. Mechanical percolation concepts have also been proposed to explain the substantial increase in viscosity, shear modulus and heat distortion temperature reported for nanotube and nanoplate filled thermoplastic polymers above the glass transition temperature.[56,57] It is important to note however that reinforcement of viscoelastic media depends on the time scale under consideration, where the critical time is characterized by the dynamics of entanglement relaxation and polymer segment interactions with the filler surface. Although the morphology of the higher loaded ZnO nanocomposites was fortuitous and not prescribed *a priori*, it provides another qualitative demonstration of the importance of achieving morphology control beyond random dispersion to optimize mechanical properties.[58,59]

Above the yield point, strain amplification in the regions surrounding the rigid filler has been shown to increase the strain-induced crystallinity of the soft-segment region of the polymer and further increase stress response with increased strain. Figure 6 summarizes WAXD for ZnO nanocomposites stretched to an elongation ratio of $\lambda = 3.5$ ($\lambda = \varepsilon + 1$, where ε is engineering strain). In all cases, the crystallinity index is the same for all loadings (~15%), which is comparable to the crystallinity index obtained for neat LHS-TPU at $\lambda = 3.5$. These results are in stark contrast to CNF filled LHS-TPU, where carbon nanofibers resulted in substantial

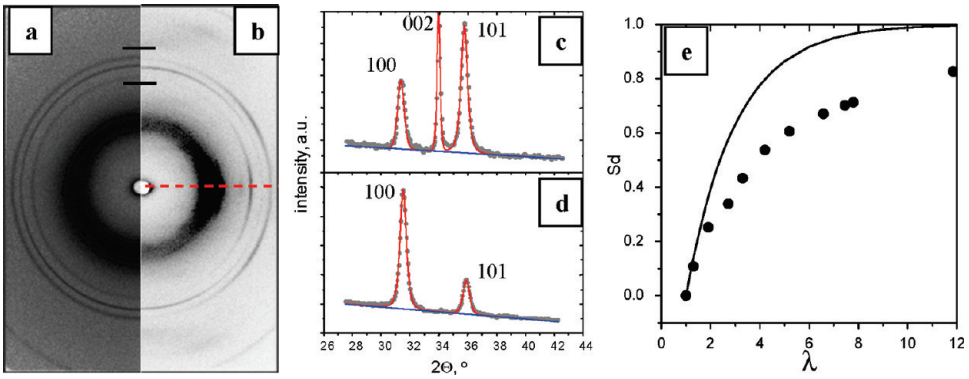

Figure 7. Two-dimensional X-ray patterns of ZnO-L2.9 nanocomposite at (a) $\lambda = 0$ and (b) $\lambda = 6$ showing alignment of ZnO with deformation, where ZnO diffraction peaks are found between the black horizontal markers. Horizontal dashed red line denotes the equatorial direction, which is perpendicular to the direction of tensile deformation. (c) Equatorial scan at $\lambda = 0$. (d) Equatorial scan at $\lambda = 6$. The 002 peak aligns along the meridian and moves out of the detector field under the experimental conditions. (e) Orientation parameter Sd[33] of d_{100} versus elongation for ZnO-L2.9 (circles). Solid line reflects the upper-bound predictions from the kinematic model for isolated rod alignment.[16,56]

increases in strain-induced crystallinity. If aspect ratio and nanoparticle loading were the only critical factors, one would anticipate at least a moderate increase in crystallinity index for the highest loading ZnO-L nanorods, even though the effective volume concentration of dispersed ZnO nanorods is lowered due to the clustered morphology. More likely is the role of the polymer nanoparticle interactions. The absence of strong hydrogen bond donor and acceptor sites on the ZnO will minimize direct interaction with the polyurethane linkages and thus reduce the efficiency of nucleating crystallites. This is consistent with the aforementioned NMR results. Thus, engineering nanoparticle−polymer interface for more than dispersion is important for impacting the intermediate strain response. Irreparable damage, such as delamination and voiding is not observed within the investigated strain range for ZnO nanocomposites, however CNF nanocomposites exhibit voiding and delamination at high elongations[16] further indicating the difference of nanoparticle polymer interaction between the two systems.

Since strain-induced crystallite content does not increase with nanorod content, changes in the higher strain behavior must be dominated by the elongational alignment of the nanorods. Figure 7 shows wide-angle X-ray diffraction (WAXD) patterns of the ZnO-L2.9 nanocomposite at two different elongations. In addition to polymer chain alignment seen at $2\theta \approx 22°$, the three major ZnO peaks (100, 002 and 101) lead to an anisotropic pattern in accordance with the alignment of a single crystal monolithic ZnO nanorod along the stretching direction. The ZnO 002 diffraction peak aligns predominantly on the meridian (deformation direction) whereas the 100 peak moves to the equator in the perpendicular direction. Furthermore, the 101 peak exhibits highest intensity at 32° from the equator in agreement with the crystallographic axis with respect to the long axis of the rod (zincite tetragonal $a/c = 1/1.6$). Parts c and d of Figure 7 show a 1D scan along the direction perpendicular to stretching, demonstrating the disappearance of the 002 diffraction peak which moves toward the meridian, whereas the 100 gains intensity and the 101 decreases.

Figure 7e compares the Herman's orientation parameter, Sd, of the ZnO NRs derived from WAXD[33] with the kinematic prediction for an isolated rod due to uniaxial deformation.[60] (Sd = 1 for perfect uniaxial order; Sd = 0 for three-dimensional random arrangement; and Sd = −0.5 for perpendicular alignment.) Sd for the ZnO nanorods approaches 0.8 at $\lambda = 10$. This is greater than previously reported for CNFs ($Sd|_{max,\ CNF} \sim 0.5$), but still less than predicted for unconstrained rod alignment. Note that the unconstrained rod prediction is determined for a single isolated rod assuming incompressibility and volume conservation. The inhibition of elongational alignment may reflect the geometrical character of the nanorods or the degree of coupling between the nanorod and matrix at the interface. For a given concentration, the smaller volume per particle and axial dimension of the ZnO nanorods relative to the CNFs result in a stiffer nanoparticle (lower aspect ratio), less particle−particle entanglement (qualitatively observed in micrographs) and a smaller volume of matrix necessary to deform to accommodate rod reorientation. Alternatively, the different behavior may reflect the lower strain-induced crystallinity in the ZnO nanocomposite, where the rod alignment would be less constrained than in the presence of large amounts of polymer crystallites that preferentially form at the CNF/polymer interface.[46] Likewise, greater chain-nanorod interactions would create nanorod−nanorod bridges through the polymer matrix, also constraining independent rotation of the nanorod. Taken together, these factors imply the ZnO nanorod orientation in the elastomeric matrix is more facile than CNF orientation.

Figure 8 shows TEM micrographs for ZnO-L2.9 and ZnO-S2.9 nanocomposites elongated to $\lambda = 8$. Images along and perpendicular to the deformation direction qualitatively confirm the high degree of ZnO nanorod alignment along the stretch direction. The degree of clustering for the short ZnO nanorods appears to be greater than for the long ZnO rods, indicating that the ZnO nanorods are associating during deformation. The strain-induced nanoparticle agglomeration leads to a hierarchical fractal network throughout the sample, that is especially visible when viewed along the stretching direction (Figure 8b). This most likely reflects the impact of nonuniform strain distribution within the matrix arising from rigid inclusions within a soft matrix, and is qualitatively consistent with concepts articulated by Boyce et al.[53] Note that due to slight section thicknesses and differences in clustering as well as tilt of nanorods it is not possible to conduct a quantitative analysis on volume fraction and particle−particle distances.

Strain-Induced Shape Memory. Previous studies demonstrated significant improvements both in the constrained shape memory fixity (the ability to hold a temporary shape) and shape memory recovery stress (the mechanical energy that can be stored) from the addition of low volume fractions (2.9 vol %) of CNF to a strain-induced shape memory LHS-TPU.[6] These enhancements were attributed to the

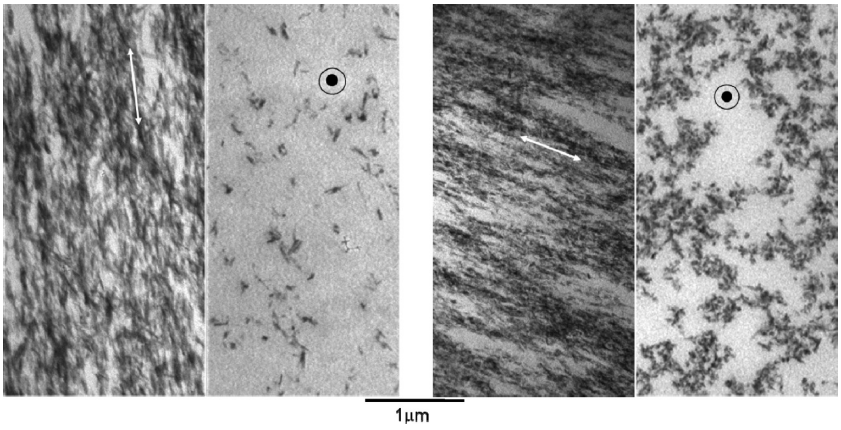

Figure 8. Transmission electron micrographs of (a) ZnO-L2.9 at $\lambda = 8$ with (left) perpendicular and (right) parallel views with respect to the stretching direction (arrow) and (b) ZnO-S2.9 at $\lambda = 8$ with (left) perpendicular and (right) parallel views with respect to the stretching direction (arrow).

Table 3. Constrained Shape Memory Fixity, f_{SM}, and Recovery Stress, s_{SM}, for ZnO-L2.9, CNF-2.9, and LHS-TPU at Different Setting Strains, λ

	constrained fixity, f_{SM}			recovery stress, s_{SM}, MPa		
setting strain	LHS-TPU	ZnO-L2.9	CNF-2.9	LHS-TPU	ZnO-L2.9	CNF-2.9
$\lambda = 2$	0.42	0.48	0.63	0.85	0.65	0.86
$\lambda = 3.5$	0.66	0.68	0.77	0.96	0.80	1.20
$\lambda = 6$	0.70	0.71	0.78	1.19	1.06	1.50

reinforcing effect of the CNFs on the elastomeric matrix; and an increase in strain-induced crystallinity that enriched the fraction of reversible cross-links (polymer crystallites) and thus retention of the elastically recoverable deformation. The latter effect implies that the overall shape memory efficiency, constrained fixity and recovery stress should increase with increasing deformation (and strain-induced crystallinity).

Table 3 compares the impact of 2.9 vol % ZnO-L on the shape memory constrained fixity, f_{SM}, and recovery stress, s_{SM}, to that of the CNFs from set strains (temporary shapes) between $\lambda = 2$ and 6. As expected, constrained fixity and recovery stress increases with increased deformation. The presence of the long ZnO nanorods at this concentration however does not increase constrained fixity relative to pure LHS-TPU at any deformation, and slightly reduces recovery stress, especially at the smaller deformations ($\lambda = 2$). This is in stark contrast to the impact of a comparable loading of CNF, which has an increasing impact on constrained fixity and recovery stress relative to LHS-TPU with increased deformation. The comparable constrained fixity between unfilled LHS-TPU and ZnO nanocomposites is consistent with the minimal effect of ZnO nanorods on strain-induced crystallization. The modest improvement of modulus with ZnO addition would be expected to provide a slight increase in recovery stress though. The decrease, although slight and approximately within experimental uncertainty, appears systematic. This may reflect the increased clustering of the ZnO at higher deformations or the very weak interface between the alkylated ZnO surface and urethane linkages, reducing stress transfer to the rigid inclusion. Further studies of the viscoplastic deformation of these systems are necessary to fully elucidate the underlying factors leading to this minor effect on recovery stress.

Table 4 summarizes the constrained shape memory fixity and shape memory recovery stress for all the ZnO nanocomposites with a set strain of $\lambda = 3.5$. Consistent with the

Table 4. Constrained Shape Memory Fixity, f_{SM}, and Recovery Stress, s_{SM}, for ZnO Nanocomposites, CNF Nanocomposites, and LHS-TPU at $\lambda = 3.5$

sample ($\lambda = 3.5$)	constrained fixity, f_{SM}	recovery stress, s_{SM}, MPa
LHS-TPU	0.66	0.96
ZnO-S0.35	0.72	0.87
ZnO-L0.35	0.64	0.81
ZnO-S2.9	0.69	0.77
ZnO-L2.9	0.68	0.80
ZnO-S12	0.81	1.54
ZnO-L12	0.88	1.79
CNF-2.9	0.77	1.20
CNF-11	0.92	2.30

performance of LHS-TPU containing 2.9 vol % ZnO-L, the recovery stress and constrained fixity for all low and intermediate loadings of ZnO is comparable to unfilled LHS-TPU. It is only at the highest loadings (12 vol %), where the ZnO morphology is hierarchical, that an increase in recovery stress σ and constrained fixity is observed. The longer rods consistently provide greater enhancement than the shorter rods, an observation that parallels the relative impact of the longer ZnO nanorods on the mechanical characteristics (Table 2). These shape memory improvements however are considerably less than observed for a comparable addition of CNFs ($s_{SM,ZnO\text{-}L12} = 1.8$ MPa, $s_{SM,CNF\text{-}11} = 2.3$ MPa), consistent with the lack of enhanced strain induced crystallites and lower flow stress after yield.

In general, the impact of ZnO on shape memory is consistent with prior studies of CNF-TPU nanocomposites in that the impact of a nanofiller on shape memory response of a strain-induced system follows the trend observed for moduli and strain-induced crystallite formation.

Conclusions

The incorporation of functionalized ZnO nanorods with two aspect ratios, ($\alpha \sim 5$, $\alpha \sim 10$) into a low hard-segment polyurethane matrix leads to mechanical and shape memory improvements only at the highest nanofiller loadings. Previous work has shown that the major factor in the shape memory enhancement of CNF ($\alpha \sim 100$) nanocomposites is the role of the nanofillers in increasing the strain-induced crystallinity of the matrix. Relative to ZnO, the CNFs exhibit a higher aspect ratio and surface groups more amenable to hydrogen bonding with the urethane linkages. NMR and WAXD investigations revealed that the alkylated ZnO nanorods do not alter matrix mobility nor act as nucleation sites for soft segment crystallites. The absence of this behavior in the nanocomposites with low ZnO loading

(< 3% v/v) is thus consistent with the minimal improvements in mechanical and shape memory properties. At the highest loadings where enhancement of strain-induced crystallinity is also absent, the formation of a hierarchical network of ZnO nanorods must be the dominating factor in the observed increase of shape memory performance of these nanocomposites. This network percolation of the nanorods conceptually provides an alternative route to shape memory enhancement.

Overall, these findings reinforce the hypothesis that the shape memory properties of polymer nanocomposites are governed by the impact of the nanoparticle on the mechanical performance and the mechanism responsible for trapping elastic strain within the host matrix. At this point though, the inability to quantitatively confirm the independent control via fabrication approaches of the numerous competing factors, including particle geometry, dispersion, morphology, and particle surface chemistry, substantially restricts the ability to establish broad, predictive conclusions that are applicable to an entire class of shape memory polymer, rather than a specific combination of nanoparticle and polymer matrix. The unique role of particle, interface, dispersion, and matrix depends on the matrix, processing history, and physical responses, including modulus, low strain behavior, yield, strain hardening, viscoplastic behavior, strain rate dependence, and recovery, that contribute to the overall shape memory response. For example, herein the broader impact of the hierarchical morphology of the higher loadings of ZnO nanorods can only be discussed speculatively. The relative importance, or more correctly the potential synergistic role, of the particle aspect ratio and interactions between the particle and matrix at the particle surface is still unclear and will require additional model systems in which these two factors can be decoupled. Nevertheless, the addition of nanoparticles provides a solid complementary route to increase the overall property suite of shape memory polymers and thus open new application opportunities.

Acknowledgment. The authors are very grateful to the Air Force Office of Scientific Research and the Air Force Research Laboratory, Materials and Manufacturing Directorate, for funding. This work was performed, in part, at the Center for Integrated Nanotechnologies, a U.S. Department of Energy, Office of Basic Energy Sciences user facility at Los Alamos National Laboratory (Contract DE-AC52-06NA25396) and Sandia National Laboratories (Contract DE-AC04-94AL85000). The authors would like to thank Gary Price for assistance in X-ray experiments and Lixia Rong at beamline X27C of the National Synchrotron Light Source at Brookhaven for help with the in situ X-ray experiments.

References and Notes

(1) Sokolowski, W.; Chmielewski, A.; Hayashi, S.; Yamada, T. Colder hibernated elastic memory (CHEM) self-deployable structures. *Proceeding of the SPIE International Symposium on Smart Structures and Materials*, Vol. *3669*, Newport Beach, CA, 1−5 March **1999**; pp 179−85.
(2) Behl, M.; Lendlein, A. *Mater. Today* **2007**, *10* (4), 20−28.
(3) Rousseau, I. A. *Polym. Eng. Sci.* **2008**, *48*, 2075–2089.
(4) Liu, C.; Qin, H.; Mather, P. T. *J. Mater. Chem.* **2007**, *17*, 1543–1558.
(5) Bassett, D. C. *Solid Phase Process. Polym.* **2000**, 11–32.
(6) Koerner, H.; Price, G.; Pearce, N. A.; Alexander, M.; Vaia, R. A. *Nat. Mater.* **2004**, *3*, 115–120.
(7) Otsuka, K., Wayman, C. M., Eds. *Shape memory materials*: Cambridge University Press: Cambridge, U.K.,1998.
(8) Zhang, D.; Leng, J.; Liu, Y. *Adv. Mater. Res.* **2008**, *47−50*, 690–693.
(9) Di Prima, M. A.; Lesniewski, M.; Gall, K.; McDowell, D. L.; Sanderson, T.; Campbell, D. *Smart Mater. Struct.* **2007**, *16*, 2330–2340.
(10) Liang, C.; Rogers, C. A.; Malafeew, E. J. *Intelligent Mater. Systems Struct.* **1997**, *8*, 380.
(11) Ash, B. J.; Stone, J.; Rogers, D. F.; Schadler, L. S.; Siegel, R. W.; Benicewicz, B. C.; Apple, T. Investigation into the thermal mechanical behavior of PMMA/alumina nanocomposites. *Materials Research Society Proceedings* **2001**, *661*, pp KK2.10.1−6.
(12) Balzar, D.; Stefanic, G.; Gall, K.; Dunn, M. L.; Liu, Y. *Adv. X-Ray Anal.* **2005**, *48*, 98–103.
(13) Gall, K.; Dunn, M. L.; Liu, Y.; Finch, D.; Lake, M.; Munshi, N. A. *Acta Mater.* **2002**, *50*, 5115–5126.
(14) Leng, J.; Lan, X.; Liu, Y.; Du, S. *Smart Mater. Struct.* **2009**, *18*, 074003.
(15) Gunes, I. S.; Cao, F.; Jana, S. C. *Polymer* **2008**, *49*, 2223–2234.
(16) Koerner, H.; Liu, W.; Alexander, M.; Mirau, P.; Dowty, H.; Vaia, R. *Polymer* **2005**, *46*, 4405–4420.
(17) Koerner, H.; White, T. J.; Tabiryan, N. V.; Bunning, T. J.; Vaia, R. A. *Mater. Today* **2008**, *11* (7−8), 34–42.
(18) Hazelton, C. S.; Arzberger, S. C.; Lake, M. S.; Munshi, N. A. *J. Adv. Mater.* **2007**, *39* (3), 35–39.
(19) Mohr, R.; Kratz, K.; Weigel, T.; Lucka-Gabor, M.; Moneke, M.; Lendlein, A. *Proc. Natl. Acad. Sci. U.S.A.* **2006**, *103*, 3540–3545.
(20) Fortener, D. *Processing and Characterization of Shape Memory Polymer Nanocomposites*, Report Number A302854, February 2006, 26 pages. http://handle.dtic.mil/100.2/ADA458203
(21) Arzberger, S. C.; Tupper, M. L.; Lake, M. S.; Barrett, R.; Mallick, K.; Hazelton, C.; Francis, W.; Keller, P. N.; Campbell, D.; Feucht, S.; Codell, D.; Wintergerst, J.; Adams, L.; Mallioux, J.; Denis, R.; White, K.; Long, M.; Munshi, N. A.; Gall, K. Elastic memory composites (EMC) for deployable industrial and commercial applications. *Proceedings of SPIE-The International Society for Optical Engineering* **2005**, *5762* (Industrial and Commercial Applications of Smart Structures Technologies), 35−47.
(22) Hsu, J. W. P.; Tian, Z. R.; Simmons, N. C.; Matzke, C. M.; Voigt, J. A.; Liu, J. *Nano Lett.* **2005**, *5*, 83–86.
(23) Wacharawichanant, S.; Thongyai, S.; Phutthaphan, A.; Eiamsamang, C. *Polym. Test.* **2008**, *27*, 971–976.
(24) Chandramouleeswaran, S.; Mhaske, S. T.; Kathe, A. A.; Varadarajan, P. V.; Prasad, V.; Vigneshwaran, N. *Nanotechnology* **2007**, *18*, 385702/385701–385702/385708.
(25) McCook, N. L.; Boesl, B.; Burris, D. L.; Sawyer, W. G. *Tribol. Lett.* **2006**, *22*, 253–257.
(26) Li, X.; Schneider, K.; Kretzschmar, B.; Stamm, M. *Macromolecules* **2008**, *41*, 4371–4379.
(27) Wu, M.; Yang, G.; Wang, M.; Wang, W.; Zhang, W.; Feng, J.; Liu, T. *Mater. Chem. Phys.* **2008**, *109*, 547–555.
(28) Zhang, T.; Xu, Z.; Qian, L.; Tao, D. L.; Teng, F.; Xu, X. R. *Opt. Mater.* **2006**, *29*, 216–219.
(29) Liu, B.; Zeng, H. C. *J. Am. Chem. Soc.* **2003**, *125*, 4430–4431.
(30) Bin Cheng, B.; Samulski, E. T. *Chem. Commun.* **2004**, 986–987.
(31) Wong, E. M.; Hoertz, P. G.; Liang, C. J.; Shi, B.-M.; Meyer, G. J.; Searson, P. C. *Langmuir* **2001**, *17*, 8362–8367.
(32) Koerner, H.; Kelley, J. J.; Vaia, R. A. *Macromolecules* **2008**, *41*, 4709–4716.
(33) Ahn, S. H.; Kim, S. H.; Lee, S. G. *J. Appl. Polym. Sci.* **2004**, *94*, 812–818.
(34) Arroyo, M.; Lo′pez-Manchado, M. A.; Valentí′n, J. L.; Carretero, J. *Compos. Sci. Technol.* **2007**, *67*, 1330–1339.
(35) Koerner, H.; Luo, Y.; Li, X.; Cohen, C.; Hedden, R. C.; Ober, C. K. *Macromolecules* **2003**, *36*, 1975–1981.
(36) Mirau, P. A. *Practical Guide to the NMR of Polymers*; John Wiley & Sons: Hoboken, NJ, 2004.
(37) Bennett, A. E.; Rienstra, C. M.; Auger, M.; Lakshimi, K. V.; Griffin, R. G. *J. Chem. Phys.* **1995**, *103*, 6951–6958.
(38) Lendlein, A.; Kelch, S. *Angew. Chem., Int. Ed.* **2002**, *41*, 2034–2057.
(39) Krishnamoorti, R.; Vaia, R. A. Polymer Nanocomposites: Synthesis, Characterization, and Modeling. *ACS Symp. Ser.* **2002**, *804*, 2002.
(40) Gujar, T. P.; Shinde, V. R.; Lokhande, C. D.; Han, S.-H. *Mater. Sci. Eng. B: Solid-State Mater. Adv. Technol.* **2006**, *133*, 177−180.
(41) Akcora, P.; Liu, H.; Kumar, S. K.; Moll, J.; Li, Y.; Benicewicz, B. C.; Schadler, L. S.; Acehan, D.; Panagiotopoulos, A. Z.; Pryamitsyn, V.; Ganesan, V.; Ilavsky, J.; Thiyagarajan, P.; Colby, R. H.; Douglas, J. F. *Nat. Mater.* **2009**, *8*, 354–359.
(42) Schadler, L. S.; Brinson, L. C.; Sawyer, W. G. *JOM* **2007**, *59*, 1047.
(43) Fornes, T. D.; Paul, D. R. *Polymer* **2003**, *44*, 3945–3961.
(44) Kelarakisa, A.; Giannelis, E. P.; Yoon, K. *Polymer* **2007**, *48*, 7567–7572.
(45) Priya, L.; Jog, J. P. *J. Polym. Sci., Part B: Polym. Phys.* **2002**, *40*, 1682–1689.

(46) Powers, D. S.; Vaia, R. A.; Koerner, H.; Serres, J.; Mirau, P. A. *Macromolecules* **2008**, *41*, 4290–4295.
(47) Thostenson, E. T.; Li, C.; Chou, T-W. *Compos. Sci. Technol.* **2005**, *65*, 491.
(48) Guth, E. *J. Appl. Phys.* **1945**, *16*, 20.
(49) Mullins, L.; Tobin, N. R. *J. Appl. Polym. Sci.* **1965**, *9*, 2993–3009.
(50) Flandin, L.; Chang, A.; Nazarenko, A.; Hiltner, E.; Baer, E. *J. Appl. Polym. Sci.* **2000**, *76*, 894–905.
(51) Fornes, T. D.; Paul, D. R. *Polymer* **2003**, *44*, 4993–5013.
(52) Guth, E.; Gold, O. *Phys. Rev.* **1938**, *53*, 322.
(53) Sheng, N.; Boyce, M. C.; Parks, D. M.; Rutledge, G. C.; Abes, J. I.; Cohen, R. E. *Polymer* **2004**, *45*, 487–506.
(54) Gusev, A. A.; Rozman, M. G. *Comp. Theor. Polym. Sci.* **1999**, *9*, 335.
(55) Stewart, R. *Reinforced Plastics* **2009**, *53* (4), 30–35.
(56) Krishnamoorti, R.; Giannelis, E. P. *Macromolecules* **1997**, *30*, 4097.
(57) Garboczi, E. J.; Snyder, K. A.; Douglas, J. F.; Thorpe, M. F. *Phys. Rev. E* **1995**, *52*, 819–828.
(58) Vaia, R. A.; Wagner, H. D. *Mater. Today* **2004**, *11*, 32–37.
(59) V. Trappe, V.; Prasad, V.; Cipelletti, L.; Segre, P. N.; Weitz, D. A. *Nature* **2001**, *411*, 772–775.
(60) Ahir, S. V.; Squires, A. M.; Tajbakhsh, A. R.; Terentjev, E. M. *Phys. Rev. B* **2006**, *73*, 085420.